Data Repository Material

Hilley, Johnson, Shen, Wang, and Bürgmann

Model Construction

Our model is a three-dimensional viscoelastic earthquake cycle model consisting of faults in an elastic lithosphere overlying a Maxwell viscoelastic asthenosphere (Johnson and Fukuda, manuscript in preparation). The model incorporates both long-term and interseismic crustal motions using the back-slip model concept that originated with Savage and Burford [1973] and Savage [1983]. The principal idea of these back-slip models is that the interseismic velocity field can be decomposed into: 1. a steady, long-term velocity field in which faults slide at the long-term slip rate, and 2. a transient perturbation to this steady-state due to locking of faults during the interseismic period. Interseismic locking of faults is modeled with backwards slip to cancel the long-term velocity discontinuity. The solution for a dislocation in an elastic half-space Savage and Burford [1973]) or in an elastic plate overlying a viscoelastic substrate Savage and Prescott [1978]) was adopted for the back-slip part of the solution. The back-slip models assume no steady-state strain in the fault bounded blocks. The 3D elastic half-space versions of this model (e.g., McCaffrey [2002], Meade and Hager [2005]) are directly analogous to the 2D elastic model of Savage and Burford [1973]. In the 3D models, fault-bounded blocks rotate undeformed over the long term about Euler poles and interseismic elastic strain is introduced with backwards slip on dislocations in an elastic half space.

We developed the solution for a dislocation in an elastic plate overlying a Maxwell viscoelastic substrate using the method of propagator matrices and the correspondence principal for viscoelasticity. The formulation is essentially identical that of to Fukahata and Matsu'ura [2006] and we refer the reviewer to this work for a mathematical formulation of the solution.

The viscoelastic block model used in this paper is analogous to the 2D Savage models for faults in an elastic layer overlying a viscoelastic half-space (Savage and Burford [1973]), Savage and Prescott [1978]). We model the interseismic deformation field as a superposition of a steady-state, long-term velocity field (with no fault locking) and an interseismic perturbation to this steady state due to periodic locking and unlocking of faults in an elastic lithospheric plate overlying a Maxwell viscoelastic asthenosphere.

Long-term, steady-state velocity field

We adopt a kinematic steady-state velocity field as an extension of elastic half-space block models developed by McCaffrey [2002] and Meade and Hager [2005]. In the elastic half-space block models, the steady-state velocity field is defined by rigid-body rotations of blocks about Euler poles which result in fault-normal and fault-parallel velocity discontinuities across faults and purely horizontal block motions. Our method is based on this idea, but we modify the block motion to remove fault-normal velocity discontinuities. Our steady-state velocity field satisfies the following slip conditions on faults: 1. the fault-normal component of velocity discontinuities across faults is zero, 2. the strike component of slip rate on faults is equal to the strike component of velocity discontinuity across faults resulting from rigid block motions. The first condition guarantees that fault surfaces do not open or inter-penetrate.

The steady-state surface velocity field is obtained by summing three separate velocity fields. We begin with rotations of blocks bounded by faults defined by Euler poles of rotation. The fault-normal components of velocity discontinuities across faults are canceled by adding the velocity field generated by steady opening or closing of the faults. The cancellation of fault normal discontinuities is computed using the solution for a dislocation with steady tensile slip in an elastic plate overlying a viscoelastic half space.

Perturbation to steady state: Earthquake cycle

Our formulation of the earthquake cycle is nearly identical to the formulation presented Matsu'ura and Sato [1989]. Areas of faults that are locked during the interseismic period are modeled with steady back-slip to cancel the long-term velocity discontinuity across the fault. Periodic earthquakes on the locked section are modeled with an infinite sequence of periodic slip events on the locked sections. Steady backslip is modeled with steady creep on a fault in an elastic plate. Periodic earthquakes are modeled by imposing an infinite sequence of sudden slip events on the faults such that the coseismic slip divided by the earthquake recurrence time is equal to the long-term fault slip rate. As shown by Matsu'ura and Sato [1989], the sum of an infinite number of solutions for a single earthquake imposed at a regular recurrence interval can be obtained analytically.

Formulation of model for Tibet

We cast surface velocities in terms of two Rotation Poles (RPs) representing rotation of the Qaidam and Songpan blocks relative to stable Tarim, and the earthquake cycle parameters, t/T and t/T. We then select fixed values for t/T and t/T, and invert the GPS velocity field for the RPs, from which slip rates along the KF and ATF are derived (described below).

We calculate velocities due to rigid-block rotations directly from the RPs, the angular location of each of the geodetic station, and the radius of the earth as described in McCaffrey [2002] and Meade and Hager (2005). This defines how rigid-body rotations within the spherical caps change with changing rotation poles. To ensure that the surface velocity distribution remains continuous at the surface, we discretize the boundaries of each of the rotating spherical caps into planar segments. During the interseismic period we impose back-slip on each segment at a rate that exactly opposes the rotation accommodated between blocks. This is accomplished by resolving the velocity due to the rotation described by the RPs onto each side of each of the planar segments to determine the relative displacement rate across each of these segments. This back-slip is imposed on a dislocation extending over the entire thickness of the elastic layer for both strike-slip and opening-mode components of the velocities. Finally, we assume that earthquake-cycle deformation occurs as the result of discrete strike-slip earthquake events along the block boundaries. At the beginning of the earthquake cycle, a uniform displacement equal to the strike-slip rate along each of the defined fault segments times the recurrence interval is imposed over the planar dislocation that extends the entire depth of the upper, elastic layer.

For simplicity, in this study, all earthquakes along all segments are synchronous and share a common recurrence interval, which does not change over time. We explored the effect that asynchronous earthquakes would have on surface velocities, which we describe below.

Surface velocities vary linearly with the components of the RPs for both the rotation and backslip components of our model, allowing us to perform a standard linear least-squares inversion of the geodetic data to determine the RPs for these components for fixed values of t/T and t /T. However, the time-dependent surface velocities are nonlinearly related to t/T and t /T. To exploit a linear inversion for this problem, we progressively fix values for t/T and t/T to specify the time-dependent, non-linear component of the modeled surface velocities and scale this contribution with the strike-slip rate that results from each component of each RP on each fault segment. This contribution is summed with that due to rigid-block rotation and backslip, and a linear inversion is performed. The best-fit RPs was used to determine the reduced chi-square statistic for the model fit to the data. Next, the values of t/T and t/T were varied, and each set of best-fit RPs was used to calculate each reduced chi-squared value as a function of t/T and t /T. From each of the best-fit RPs, the slip rates along the ATF and KF were determined by resolving the surface velocities due to the rotations onto the fault segments.

In our model, we specified all earthquakes along fault segments to be synchronous. In addition, we considered only a single lower viscoelastic layer of infinite extent in our modeling. Both of these factors are clearly oversimplifications. We explored the first of these effects by systematically varying the value of t/T for each segment. We found that when t /T was large, a spatially varying t/T did not appreciably impact the velocity field. However, as t /T was decreased, surface velocities along different segments became quite variable depending on the relative time in the earthquake cycle. This caused modeled surface velocities to vary significantly in space, depending on the time since the last earthquake along each of the segments. In contrast, the observed surface velocities are continuous in space and do not show the significant excursions expected when lower layer viscosities are low and t/T varied appreciably between fault segments. Thus, either t /T is small and t/T is the same, or t /T is large when viewed in the context of our simple two-layer model. This lends further support to the hypothesis that t /T is likely large in the area, or else it is very coincidental that we do not see such pronounced variations in space that might be expected if t /T was small and t/T was variable for each of the segments. In the end, we chose not to include the results of this modeling in the text, because of the lack of high-quality paleoseismic data along these faults that would be required to perform a meaningful calibration of the model in which t/T was allowed to vary according to each segment.

The second assumption of our model is that the lower viscoelastic layer extends to an infinite depth. In Tibet, a layered viscosity structure may be appropriate based on some geodynamic models of the area (e.g., Royden et al., 1996). Based on our previous work in the Mojave, such layering could mask the presence of a low viscosity zone in the lower crust of Tibet. However, such masking does not affect our conclusion that viscoelastic earthquake cycle effects cannot be invoked to reconcile high geologically determined slip rates with low geodetically measured surface velocities in the region.

Lateral contrast in lithosphere thickness

It has been proposed that the any low viscosity channel under Tibet does not extend into the Tarim basin to the north of the ATF. Therefore our simplified 3D block model with a uniform elastic thickness and uniform schizosphere viscosity may not be completely analogous to the conditions of the lithosphere surrounding the ATF. Here we utilize a boundary element model to examine the influence of a change in elastic lithosphere thickness across the fault on the surface velocity pattern.

As illustrated in Figure DR2, we model an infinitely long strong strike-slip fault in elastic lithosphere overlying a Maxwell viscoelastic asthenosphere. As in the 3D models, the fault is locked during the interseismic period and sudden periodic slip is imposed on the fault to represent earthquakes. We model a 2000 km-wide shear zone in which we impose half the long-term fault slip rate at both ends of the elastic lithosphere such that the fault slips to keep up with the relative motion of the edges of the shear zone. The upper ground surface is traction-free. For simplicity, the edges of the asthenosphere are also assumed to be traction free, however the results are generally not sensitive to the choice of boundary conditions for the edges of the asthenosphere.

Figure S3 illustrates velocity profiles generated with the variable-thickness boundary element model assuming the geometry shown in Figure DR2. Profiles are shown for two different ratios of recurrence time of earthquakes, T, to relaxation time of asthenosphere, t and for different times, t, since the last earthquake. For comparison, the Savage and Prescott [1978] model with an elastic plate of uniform thickness of 15 km is shown for the same earthquake timing parameters. Surface velocities scale linearly with fault slip rate, so normalized surface velocities are plotted. The lithospheric thickness change across the faults introduces an asymmetry in surface velocities that are more pronounced for smaller t/T ratios (lower viscosity asthenosphere or longer recurrence times). Strain rates are generally lower on the side of the fault with the thicker lithosphere. The surface velocities at a distance of 500 km from the fault are similar for the uniform thickness and variable thickness models, however the shape of the velocity profiles are different.

As an idealized analog for the ATF bounded by the thick crust of the Tarim Basin and the perhaps thinner crust of the Tibetan Plateau, we use the model geometry illustrated in Figure DR2. We assume the last large earthquake on the ATF occurred 600 years ago with an earthquake recurrence time of 1000 years (e.g., Washburn et al., 2001). Figure S3 shows fault-parallel GPS velocities at sites near the center of the ATF projected onto a profile perpendicular to the fault as well as model velocity profiles for different asthenosphere viscosities. The error bars on the data are 1s. For each asthenosphere viscosity shown in Figure S3, we have adjusted the fault slip rate by eye to best match the observed velocity profile in a qualitative sense. The curves are labeled with this slip rate.

The data are not of sufficiently high quality to determine the degree of asymmetry in velocity profile across the ATF. The model curves show that the data are reasonably well reproduced with the variable-thickness model for asthenosphere relaxation times of 2×10^{19} Pa s or higher and slip rates of 10-12.5 mm/yr. The model with asthenosphere viscosity of 10^{19} Pa s displays a degree of asymmetry in velocity profile that is perhaps not seen in the data, but is right at the edge of what can be inferred given the low signal to noise ratio of the data.

To examine the extent to which neglecting lateral variations in lithosphere thickness in our 3D models might bias estimates of fault slip rate, we conduct synthetic inversions. We generate two synthetic data sets using the boundary element model surface velocity profiles for asthenosphere viscosities of 2×10^{19} Pa s and 10^{20} Pa s, recurrence time of 1000 years, time since last earthquake of 600 years, and slip rate of 15 mm/yr. The lithosphere geometry is as shown in Figure DR2. We add Guassian noise to the data and invert for fault slip rate, elastic thickness and recurrence time using the Savage and Prescott [1978] model assuming the time since the last earthquake is known. The Savage and Prescott [1978] model is analogous to our 3D earthquake cycle model, so this serves as a logical test of the model assumptions in our model for Tibet. The synthetic data sets are shown in Figure S5. We estimate posterior probability distribution for parameters using a Monte Carlo-Metropolis sampling algorithm and the marginal posterior distributions for parameters are shown as histograms in Figure S5. The ‘true’ values are shown with green bars. The important result is that the estimate fault slip rates are only slightly lower than the true slip rates (within 90% of the true values). Therefore we conclude that the fault slip rate inferences from the 3D earthquake cycle model that we use in this paper are not significantly biased by our assumption of uniform elastic thickness.

Data Processing

We reprocessed data from 21 GPS station locations reported in Bendick et al. (2000) and Wallace et al. (2005) to integrate these velocities into the ITRF2000 reference frame. These data were processed together with Asia fiducial sites (IGS for 1994 and 1998; IGS+CMONOC for 2002) using GAMIT, using loosely constrained daily solutions are output for site positions, orbits, and pmu parameters. Reprocessed GPS sites are listed in Table 1, while fiducial sites are listed in Table 2. The above solutions were combined with SOPAC loosely constrained daily global solutions using GLOBK, and combined loosely constrained daily solutions were output with orbital parameters surpassed.

During the observation period, the 2001 Kokoxili earthquake resulted in coseismic ground deformation that required adjustments of the observed surface positions. To do this, coseismic displacements for the 2001 Kokoxili earthquake were calculated at sites using a fault slip model obtained through inversion of GPS and observed surface slip data. The daily SINEX files were modeled to estimate site positions, velocities, and coseismic deformation using QOCA. A group of IGS sites were constrained to their ITRF2000 velocities with uncertainties of 2, 2, and 5 mm/yr for the east, north, and up components respectively. The coseismic deformation due to the 2001 earthquake was constrained by the prior estimates of the modeled surface deformation field using the following uncertainties: $\sqrt{(0.6D_i)^2 + (0.3D_j)^2 + (0.3D_k)^2}$, where D_i, D_j, and D_k are the uncertainties in the coseismic displacements in the x, y, and z directions, respectively.

Once the ITRF2000-referenced surface velocity field was computed (presented in Table 3), we used a set of sites within the interior of the Tarim Basin (listed in Table 4) to determine the best-fitting rotation pole of this block. All station velocities were adjusted to this rotation pole to form a Tarim-Basin-based reference system, within which the modeling was carried out. GPS velocities referenced to this rotation pole are reported in Table 5.

SOM Table DR1: Reprocessed Site Names from Bendick et al. (2000) and Wallace et al. (2005)

GRUB	ATUB	SLUB
QUIS	MANG	COOL
HATU	MULI	TERR
HAPI	SCAS	SCAN
KLSA	NICE	PAXI
SFER	POWR	ROQG

MILA	HOTL	LOBU

SOM Table DR2: Feducial Site Names

Y348	AL10	JB46
AL23	G171	I035
JB32	AL35	G172
AL03	I034	

SOM Table DR3: Reprocessed Sites in ITRF2000 Reference Frame

Longitude (°)	Latitude (°)	E velocity (cm/yr)	N Velocity (cm/yr)	1-sigma E Velocity(cm/yr)	1-sigma N Velocity(cm/yr)	Correlation Coefficient	Station Name
88.153	39.030	0.07	0.83	0.22	0.22	0.011	ROQG
88.265	39.446	0.26	0.88	0.13	0.13	-0.005	LOBU
88.849	39.027	0.03	0.80	0.23	0.23	0.002	POWR
88.898	39.243	-0.33	0.77	0.47	0.35	-0.256	HOTL
88.899	39.241	0.33	0.68	0.13	0.13	-0.002	MILA
89.056	38.968	0.07	0.82	0.24	0.25	0.001	SFER
89.282	38.614	-0.24	-0.04	0.14	0.14	-0.005	PAXI
89.630	38.468	0.47	0.69	0.14	0.14	-0.005	NICE
89.905	38.409	0.62	0.80	0.14	0.14	-0.005	KLSA
89.926	38.409	0.59	0.77	0.15	0.15	-0.017	SCAN
89.932	38.404	0.64	0.83	0.23	0.18	-0.127	SCAS
89.968	38.391	0.70	0.91	0.14	0.14	-0.003	HAPI
90.085	38.391	0.74	0.98	0.14	0.13	-0.006	TERR
90.131	38.031	0.61	1.00	0.38	0.41	0.001	COOL
90.418	38.376	0.96	0.89	0.14	0.14	-0.010	MULI
90.907	38.285	0.76	0.79	0.14	0.14	-0.006	HATU
91.821	37.887	1.16	0.97	0.15	0.14	-0.006	MANG
85.143	37.124	0.18	1.08	0.18	0.19	0.014	SLUB
85.144	37.057	-0.03	1.34	0.17	0.17	0.006	ATUB
85.428	37.582	-0.09	1.17	0.17	0.17	0.011	QUIS
85.156	36.986	0.15	1.42	0.18	0.18	0.006	GRUB
85.456	37.387	0.05	1.14	0.17	0.17	0.014	AQIN

SOM Table DR4: Sites Used to Define Tarim Reference (Reported Locations in Zhang et al., 2005)

G122	G123	I033
I063	I064	I065
I075	I077	I079
I081	I082	I083
I084	I086	I087

SOM Table DR5: Sites in Tarim-Block-Based Reference Frame Used in Modeling

Longitude (°)	Latitude (°)	E velocity (mm/yr)	N Velocity (mm/yr)	1-sigma E Velocity(mm/yr)	1-sigma N Velocity(mm/yr)	Correlation Coefficient	Station Name
89.926	38.409	3.90	1.44	1.50	1.50	-0.017	SCAN
93.003	39.287	0.74	0.24	1.20	1.10	0.003	G165
93.489	39.645	-0.93	-0.37	1.20	1.10	0.010	G163
94.555	39.716	0.36	2.60	1.40	1.20	0.011	G162
94.857	39.514	1.56	0.94	1.40	1.20	0.010	G164
94.998	40.549	-1.79	0.36	1.20	1.10	0.010	G160
94.813	40.172	-0.51	1.91	1.20	1.10	0.007	G161
89.905	38.409	4.20	1.73	1.40	1.40	-0.005	KLSA
89.630	38.468	2.66	0.40	1.40	1.40	-0.005	NICE
89.282	38.614	-4.56	-7.18	1.40	1.40	-0.005	PAXI
91.083	38.764	2.37	0.58	2.10	2.10	0.003	AL03
88.898	39.243	-6.06	0.61	4.70	3.50	-0.256	HOTL
89.196	38.717	-1.36	0.95	1.40	1.40	0.003	G172
89.056	38.968	-1.80	1.24	2.40	2.50	0.001	SFER
86.251	38.077	-2.86	6.59	2.40	2.30	0.002	G0BB
86.977	38.508	-1.16	-0.03	1.60	1.60	0.004	I035
87.072	38.709	-1.07	1.05	1.60	1.50	0.005	AL35
88.153	39.030	-1.79	0.61	2.20	2.20	0.011	ROQG
88.265	39.446	-0.32	1.20	1.30	1.30	-0.005	LOBU
88.899	39.241	0.54	-0.29	1.30	1.30	-0.002	MILA
88.849	39.027	-2.24	0.87	2.30	2.30	0.002	POWR
88.184	39.024	-2.39	-0.66	1.60	1.60	0.003	I034
87.194	40.835	-0.41	-0.36	1.20	1.10	0.005	I032
85.456	37.387	-0.10	1.55	1.70	1.70	0.014	AQIN
85.428	37.582	-1.69	1.83	1.70	1.70	0.011	QUIS

83.811	37.594	0.38	-1.35	1.50	1.10	-0.020	I066
82.696	37.046	2.66	-0.03	1.70	1.20	-0.011	I067
85.538	38.081	-1.10	-0.48	1.30	1.30	0.005	JB46
84.850	37.242	-4.19	4.67	2.40	2.20	0.011	Y348
94.873	36.433	10.76	4.96	1.00	1.00	-0.004	JB30
98.462	36.943	8.52	5.38	1.10	1.00	-0.013	G159
98.345	37.307	6.15	5.29	1.20	1.10	0.003	G154
96.699	37.363	5.59	6.84	1.60	1.20	0.003	G156
98.854	37.979	4.07	2.70	1.10	1.10	0.001	G149
98.657	37.578	7.98	3.94	1.20	1.10	0.003	G150
95.803	37.513	6.55	3.61	1.40	1.20	0.009	G151
94.998	38.057	4.82	3.26	1.40	1.20	0.013	G169
93.499	37.902	7.22	2.74	1.50	1.20	0.017	G170
94.355	38.809	3.28	3.13	1.40	1.20	0.010	G167
97.378	37.381	7.17	4.00	0.90	0.90	-0.002	DLHA
93.412	38.809	4.91	1.07	1.00	1.00	-0.001	JB31
90.442	37.274	5.90	6.96	1.90	1.70	0.004	Y196
91.821	37.887	10.01	4.98	1.50	1.40	-0.006	MANG
91.914	38.091	6.80	4.15	2.80	2.50	0.001	AL23
90.804	38.287	5.36	4.15	1.50	1.40	0.002	G171
90.907	38.285	5.66	2.44	1.40	1.40	-0.006	HATU
90.131	38.031	4.46	3.91	3.80	4.10	0.001	COOL
90.418	38.376	7.60	3.04	1.40	1.40	-0.010	MULI
89.968	38.391	5.01	2.88	1.40	1.40	-0.003	HAPI
90.085	38.391	5.40	3.67	1.40	1.30	-0.006	TERR
89.932	38.404	4.40	2.05	2.30	1.80	-0.127	SCAS
90.982	38.588	4.05	2.80	1.40	1.30	0.004	JB32
85.144	37.057	-0.54	3.31	1.70	1.70	0.006	ATUB
85.143	37.124	1.50	0.71	1.80	1.90	0.014	SLUB
92.036	31.469	25.79	9.17	1.33	1.14	0.013	NAGQ
94.097	31.917	25.83	2.92	1.40	1.10	0.006	J019
97.169	31.162	21.34	-2.97	1.30	1.10	0.000	J010
98.209	34.894	16.38	4.77	1.20	1.10	0.002	J005

96.988	32.997	22.50	1.28	1.10	1.00	-0.001	JB49
91.985	32.986	21.13	5.31	1.10	1.00	-0.001	JB52
91.693	32.275	23.51	7.04	1.18	0.93	0.041	ANDU
91.858	33.234	24.47	7.38	1.06	0.92	0.012	TANG
92.056	33.649	22.41	5.46	1.20	0.96	0.018	YANS
92.447	34.214	23.15	1.66	1.90	1.35	0.071	TUOT
92.854	34.631	20.28	3.36	2.67	2.07	0.035	ERDA
93.052	35.088	16.97	3.37	1.00	1.00	-0.005	JB51
93.913	35.520	16.11	2.92	3.72	2.65	0.067	BUDO

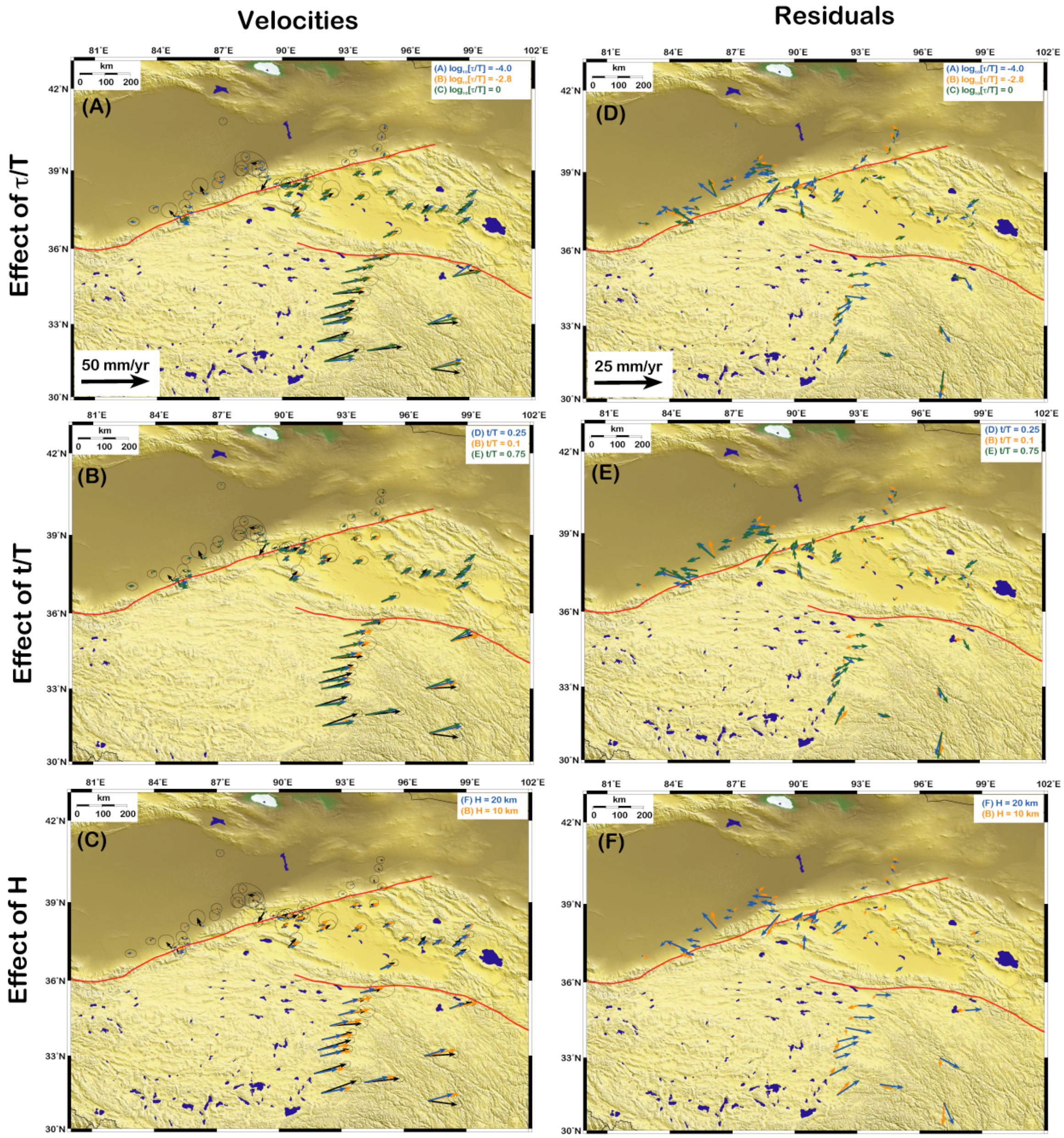

Figure DR1: Observed and modeled surface velocities (A-C) and vector difference between observed and modeled velocities (residuals; D-F) for scenarios shown in Figure 2. The first column highlights the impact of changing t/T, the second t/T (B, E) and the third H (C, F).

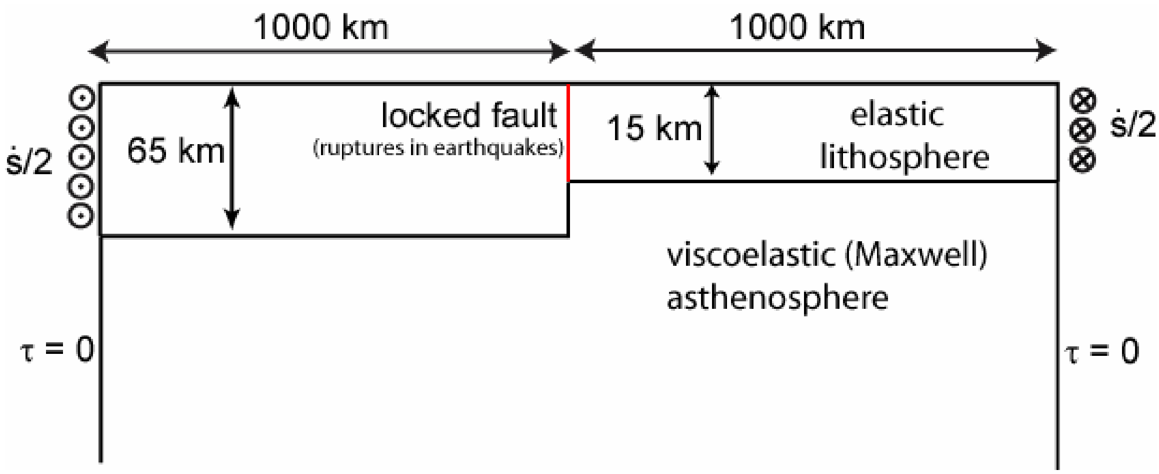

Figure DR2. Illustration of boundary element model designed to examine the influence of variable elastic thickness on surface velocity pattern. The model is antiplane strain (all motions in and out of paper). Red fault is infinitely long strike-slip fault with imposed periodic earthquakes. Fault is locked between earthquakes. A 2000 km-wide shear zone is driven at constant far-field relative velocity of 15 mm/yr.

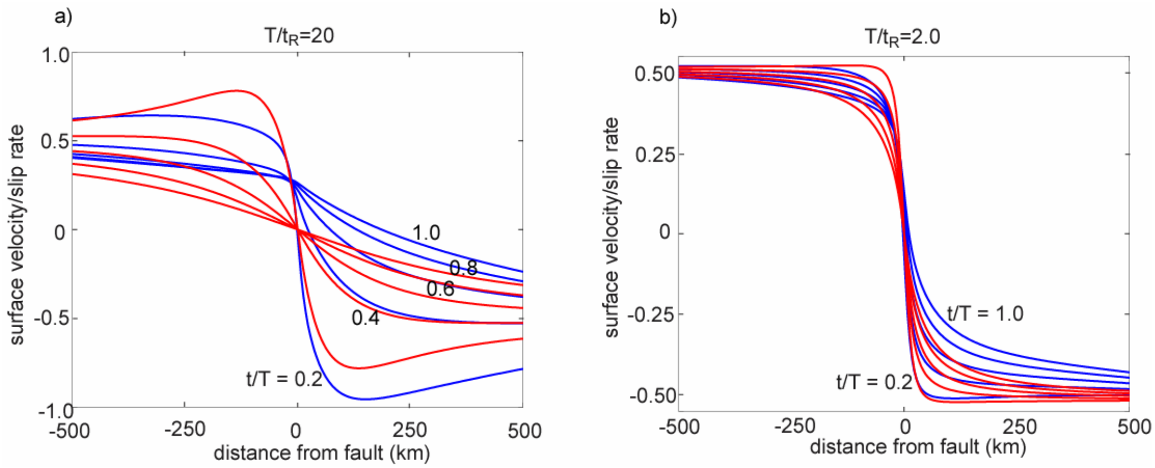

Figure DR3. Surface velocity profiles generated with boundary element model shown in Figure DR2 (blue curves). Profiles are shown for two different ratios of recurrence time, T, to relaxation time, t, and at different times since the last earthquake, t. For comparison, surface velocities predicted by the Savage and Prescott [1978] model are shown in red for the same earthquake times, relaxation times, and elastic plate thickness of 15 km. Surface velocities are normalized by fault slip rate. The asymmetry in the velocity profiles introduced by abutting plates of different thickness is more pronounced for the lower viscosity case (a).

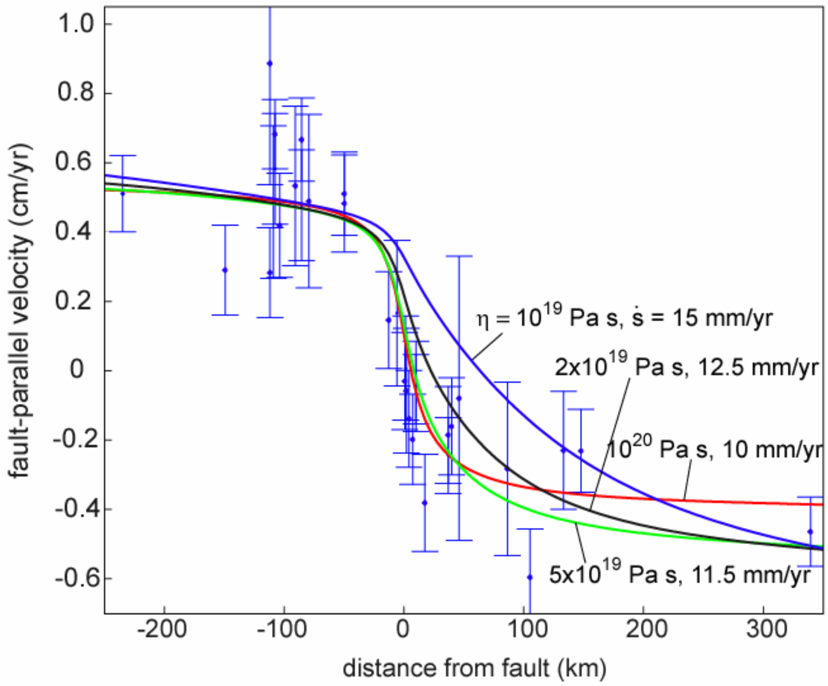

Figure DR4. Profile of GPS velocities across central part of ATF. Error bars are 1s uncertainties. Curves are surface velocity profiles generated with the variable lithosphere thickness model in Figure DR2. The curves are generated assuming a periodic earthquake recurrence interval of 600 years and 300 years since the last earthquake. Slip rate is adjusted “by eye” to qualitatively fit the GPS data. Lithosphere geometry is shown in Figure DR1 and curves are labeled with asthenosphere viscosities and slip rates.

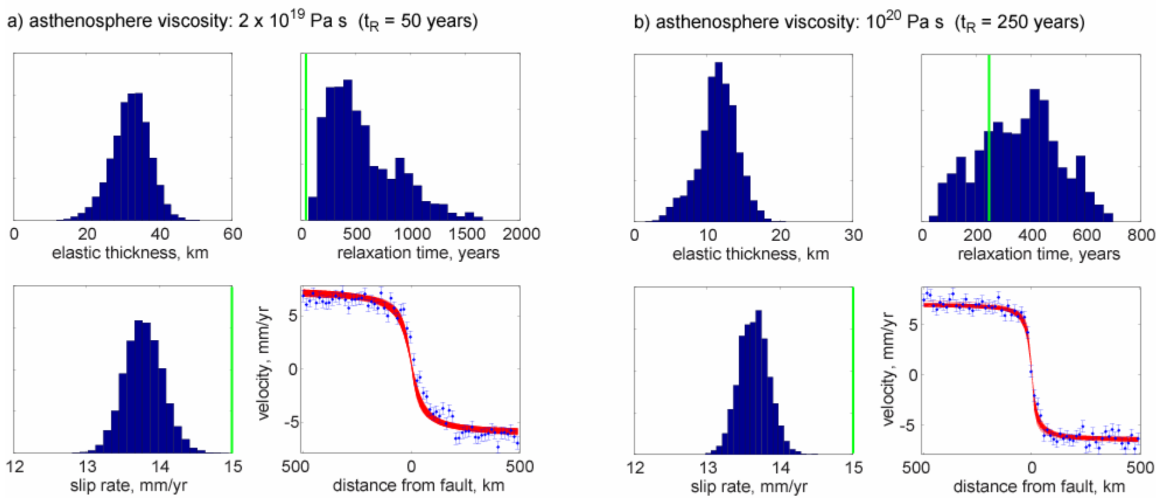

Figure DR5. Synthetic inversion results. Guassian noise was added to profiles shown in Figure S3 and synthetic data were inverted for parameters assuming the Savage and Prescott [1978] earthquake cycle model. Time since last earthquake is assumed known and other parameters are estimated using a Monte Carlo-Metropolis inversion. Histogram plots represent posterior probability distributions of parameters. Synthetic data with 2s uncertainties and shown in bottom right panels. Red curves are posterior 2s model predictions.